Air–Sea Heat Exchange along the Northern Sea Surface Temperature Front in the Eastern Tropical Pacific

NICOLAI THUM, STEVEN K. ESBENSEN, AND DUDLEY B. CHELTON

College of Oceanic and Atmospheric Sciences, Oregon State University, Corvallis, Oregon

MICHAEL J. MCPHADEN

NOAA/Pacific Marine Environmental Laboratory, Seattle, Washington

(Manuscript received 25 June 2001, in final form 12 June 2002)

ABSTRACT

The atmospheric response to the oceanic forcing in the eastern Pacific along the northern equatorial sea surface temperature (SST) front is investigated in terms of sensible and latent heat flux during the 6-month period from 28 July 1999 to 27 January 2000 and the 7-month period from 28 June 2000 to 27 January 2001. Of particular interest is the atmospheric boundary layer (ABL) response to oceanic tropical instability waves (TIWs) that distort the SST front during May–January in normal years. In previous studies, time series of surface heat fluxes clearly show the influence of TIWs, but the relationship to spatial patterns of SST and wind speed has been inferred only from sparse in situ data.

In this study, satellite observations are used as a basis for compositing in situ data from moorings to compensate for the lack of a spatially dense mooring array. The variability in the position of the SST front caused by westward-propagating TIWs enables fixed mooring locations to measure the ABL response from a large range of locations relative to the front. The satellite data enable determination of the precise location of the mooring relative to the front. The advantage of this strategy is the recurring measurement of the ABL response to the SST front over the 13-month period considered here.

The results indicate that the TIW-induced perturbations of sensible heat flux are spatially shifted in phase toward the east relative to the perturbations of SST. The maximum fluxes of sensible heat are not centered directly over the warmest water, but are shifted toward the portion of the frontal region where a disequilibrium boundary layer is expected due to the advection of colder air from the equatorial region. The latent heat flux pattern is approximately in phase with the SST, with only a slight shift to the east. The changes of sensible and latent heat fluxes across the SST front have typical magnitudes of about 12 and 125 W m^{-2}, respectively.

The sensible and latent heat flux patterns are interpreted in two complementary ways: 1) as an atmospheric response to the change of oceanic forcing as air flows across the SST front, and 2) as the atmospheric response to westward-propagating TIWs along the SST front.

1. Introduction

Air–sea interaction in the eastern tropical Pacific Ocean has been a topic of great interest for many years because of its significance to the global climate. In the atmosphere, the equatorial region between 15°N and 15°S is characterized by the confluence of the Northern and Southern Hemisphere trade wind regimes into the intertropical convergence zone (ITCZ). The ITCZ undergoes an annual march with the strongest convection in March being relatively symmetric about the equator, sometimes with a double ITCZ, one in each hemisphere. The ITCZ then migrates northward during the transition to Northern Hemisphere summer and remains between 5° and 10°N until almost the end of the year (Mitchell and Wallace 1992). In the eastern Pacific Ocean, the cold tongue is weakest during March, when the convergence of the trade winds is closest to the equator and the atmospheric cross-equatorial flow is weak. In September when the ITCZ is displaced farthest northward, the cold tongue and the atmospheric cross-equatorial flow are strongest (Mitchell and Wallace 1992). Although the annual cycle of incident solar radiation is symmetric about the equator, the mean atmospheric circulation in the eastern tropical Pacific is asymmetric and the region of deepest convection is found north of the equator in the climatological average. The southeasterly trade winds cross the equator and turn anticyclonically toward Mexico and Central America, and converge in the ITCZ. The location of the ITCZ and the structure of the cold tongue/ITCZ complex have been subjects of numerous studies (e.g., Mitchell and Wallace 1992; Xie

Corresponding author address: Steven K. Esbensen, College of Oceanic and Atmospheric Sciences, Oregon State University, 104 Ocean Admin. Building, Corvallis, OR 97331-5503.
E-mail: esbensen@coas.oregonstate.edu

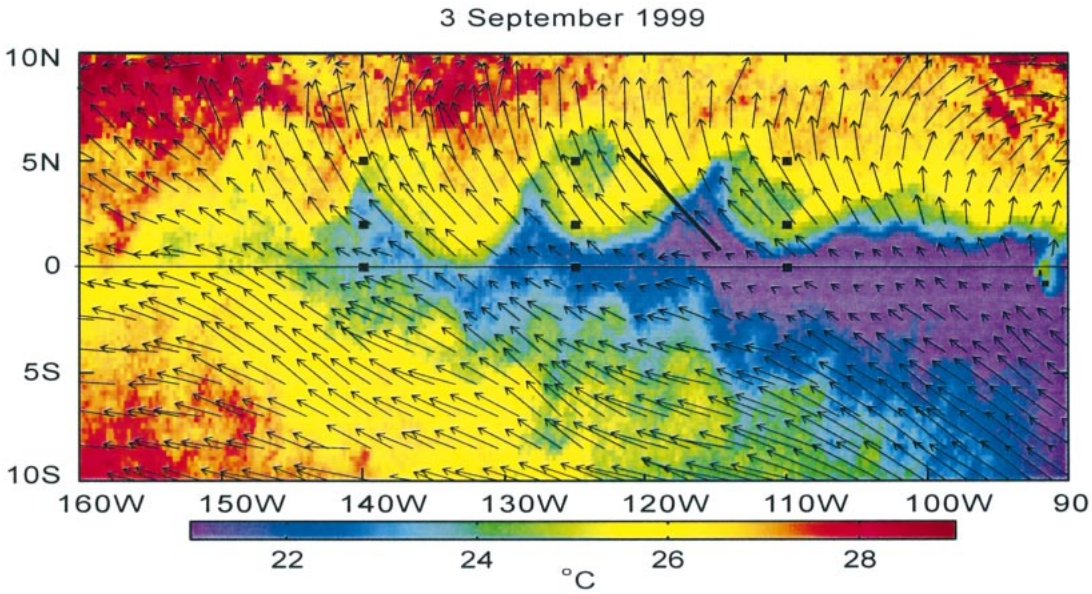

FIG. 1. Three-day average map over the period 2–4 Sep 1999 showing SST (color), wind stress (vectors), and TAO mooring locations (squares). An idealized ABL column trajectory is indicated as diagonal bar.

and Philander 1994; Philander et al. 1996) and there is ongoing debate whether the large-scale dynamics also play a significant role in determining the location of the ITCZ (see discussion in Tomas et al. 1999).

The atmospheric boundary layer (ABL) from the equator to 5°N is an important component of the cold tongue–ITCZ complex because 1) ITCZ inflow effects through airmass modification, and 2) wind stress and heat flux forcing of the upper ocean. This particular region of the eastern tropical Pacific is characterized by a strong SST gradient defining the northern flank of the cold tongue and by the oceanic tropical instability waves (TIWs) perturbing the SST front during May–January (see Fig. 1). TIWs are generated by the strong shear in the equatorial oceanic current system. These oceanic waves propagate westward with phase speeds of ~0.5 m s^{-1}, periods of 20–40 days, and wavelengths of 1000–2000 km (Qiao and Weisberg 1995).

The prevailing wind in the ABL across the northern SST front during the TIW season from May to January is southeasterly, from cold to warm water. The wind direction suggests advection of cold boundary layer air across the sharp SST front into the region of warm surface water. In this scenario, the air–sea temperature difference is increased over the warm water, indicating strong air–sea interactions. Bond (1992) suggested that air–sea fluxes lead to a reduction of low-level wind shear north of the cold tongue. This reduction of wind shear is thought to be at least partly caused by a reduction of static stability and enhanced horizontal momentum mixing on the warm side of the front. The enhanced downward mixing of horizontal momentum accelerates the wind to the north of the front and the pattern of wind stress changes significantly across the SST front. We will refer to this as the ABL momentum mixing hypothesis. Mean values of wind stress over a 3-month period from July to October 1999 of less than 0.02 N m^{-2} are found over the cold tongue, increasing to more than 0.08 N m^{-2} over the warm water (Chelton et al. 2001).

Such coupling between the atmospheric boundary layer and the TIW SST patterns should result in distinctive patterns of wind stress and other meteorological features that propagate to the west with the TIW-induced SST perturbations. Using satellite observations of low-level cloud coverage, Deser et al. (1993) found that large values of cloud reflectivity were observed over and upstream of the warm SST anomalies. Using satellite observations of SST and wind, Xie et al. (1998) found that the wind divergence field was highly correlated with the TIW SST anomaly patterns, resulting in phase-locked centers of ABL wind divergence and convergence that propagate westward with the TIWs.

With the availability of high-resolution satellite wind and SST data, Chelton et al. (2001) were able to investigate in detail the dependency of the wind stress divergence and curl fields on the angle between the SST gradient vector and the wind stress. SST and wind stress fields were zonally high-pass filtered to remove the large-scale background variability with zonal wavelengths longer than 20°. The anomalous wind stress divergence in the TIW region was found to be proportional to the downwind component of the SST anomaly gradient, while the anomalous wind stress curl was proportional to the anomalous cross-wind component of the SST gradient. These robust relationships were found to persist throughout the period of strong TIW activity.

The phase relation between SST and latent heat fluxes

were described by Liu et al. (2000). The latent heat flux was inferred from remotely obtained SST, wind speed, and integrated water vapor using the methodology developed by Liu (1988). They showed that latent heat flux is in phase with SST and wind speed, but the magnitude of the variations could not be determined with confidence due to the inaccuracy of the latent heat flux calculation on time periods shorter than 10 days (Liu et al. 1991).

A remote influence of TIWs to the variability of the hydrological variables of integrated water vapor, cloud liquid water, and precipitation a few degrees north of the SST front was shown by Hashizume et al. (2002). The patterns of these variables north of 6°N are shifted toward the west relative to the pattern of SST. Increased water vapor, liquid water, and rain are found in regions of wind convergence.

The association of accelerating surface winds with strong downwind SST gradients suggests the possibility of strong air–sea heat exchange. Zhang and McPhaden (1995) pointed out that as surface winds cross the SST front toward warmer water to the north of the cold tongue, surface sensible heat and evaporation increase greatly. They estimated a change in latent heat flux of about 50 W m^{-2} (1 K)$^{-1}$ change in SST. The reduction in solar radiation due to enhanced low-level cloudiness over the warm water was estimated by Deser et al. (1993) to be about 25 W m^{-2}. A more detailed analysis of the latent and sensible heat fluxes in relation to the SST pattern can provide further insight into the mechanisms that modify ABL structure across the SST front.

In this study, estimates of surface sensible and latent heat fluxes are calculated from the surface and near-surface in situ measurements provided by the Tropical Ocean Global Atmosphere (TOGA) Tropical Atmosphere Ocean (TAO) mooring array (McPhaden et al. 1998). Remotely sensed data are used to establish the relationship between SST and wind patterns and the TAO time series at nine mooring locations (0°, 2°, and 5°N at 140°, 125°, 110°W). Through compositing, the in situ and remotely sensed observations of heat flux and wind stress can be *collectively* interpreted as a response to recurring TIW patterns of SST. Two compositing techniques are used to answer the following questions about the ABL response: 1) How does an idealized ABL air column respond when crossing the SST front near 2°N? 2) What is the spatial and temporal relation between the responses at 2° and 5°N for a typical wave cycle?

The datasets that were used for the analysis are summarized in section 2, followed by descriptions of the data processing issues, heat flux calculations, and compositing methods in section 3. In section 4, the results of the two compositing methods are presented separately, while in section 5 the compositing methods are interpreted in combination to develop a detailed picture in terms of magnitude and regional distribution of air–sea heat exchanges.

2. Data description

This study uses independent observations of SST, wind stress, and surface meteorological variables from satellite and buoy systems. The analysis benefits from the individual advantages of the observational platforms. The in situ measurements from the TAO mooring array provide the crucial surface and near-surface measurements of meteorological variables that are needed to calculate reliable estimates of sensible and latent heat flux. The satellite data allow the placement of the buoy point measurements in their spatial context relative to the TIW perturbations of SST and wind (Fig. 2).

The availability of wind stress data from the QuikSCAT instrument during the 1999–2000 TIW season restricts the analyzed time period. We have chosen the 28 July 1999–27 January 2000 time period for the 1999–2000 TIW season and the 28 June 2000–27 January 2001 time period for the 2000–2001 TIW season for the analysis presented here.

The buoy measurements from the TAO mooring array provide the in situ dataset consisting of SST at 1-m depth, air temperature and relative humidity at 3-m height, and the wind speed and direction at 4-m height. Daily averaged data were used to resolve the atmospheric response to the oceanic forcing by TIWs that have periods of 20–40 days. Since this investigation is focused on the ABL response to SST perturbations resulting from TIWs, nine buoy locations along 0°, 2°, and 5°N at 140°, 125°, and 110°W were chosen, covering the region of high TIW variability (see Figs. 1, 2a, black squares indicate buoy locations).

Detailed spatial information is obtained from the combined use of satellite-observed SST and wind stress. The SST data are provided by the Tropical Rainfall Measuring Mission (TRMM) Microwave Imager (TMI) on board the TRMM satellite (Kummerow et al. 1998; Chelton et al. 2000). These data were analyzed to provide 3-day mean fields with a spatial resolution of 46 km. The TMI SST measurements are based on the 10.7-GHz brightness temperature that has a very small atmospheric contribution, except for heavy rain measurements that are flagged and excluded from further analysis. The SST measurement accuracy has been shown to be better than 0.5°C for the region of interest here (Chelton et al. 2001).

Surface wind stress was measured by the SeaWinds scatterometer on board the QuikSCAT satellite. The QuikSCAT data record analyzed here begins on 28 July 1999. The instrument provides wind stress estimates with a 25-km resolution over a single 1600-km swath that is then interpolated and smoothed to obtain daily maps of overlapping 3-day averages on a 0.25° spatial grid (Freilich 1996; Spencer et al. 1997).

3. Methodology

The buoy time series of meteorological variables suggest a strong influence of TIWs on atmospheric bound-

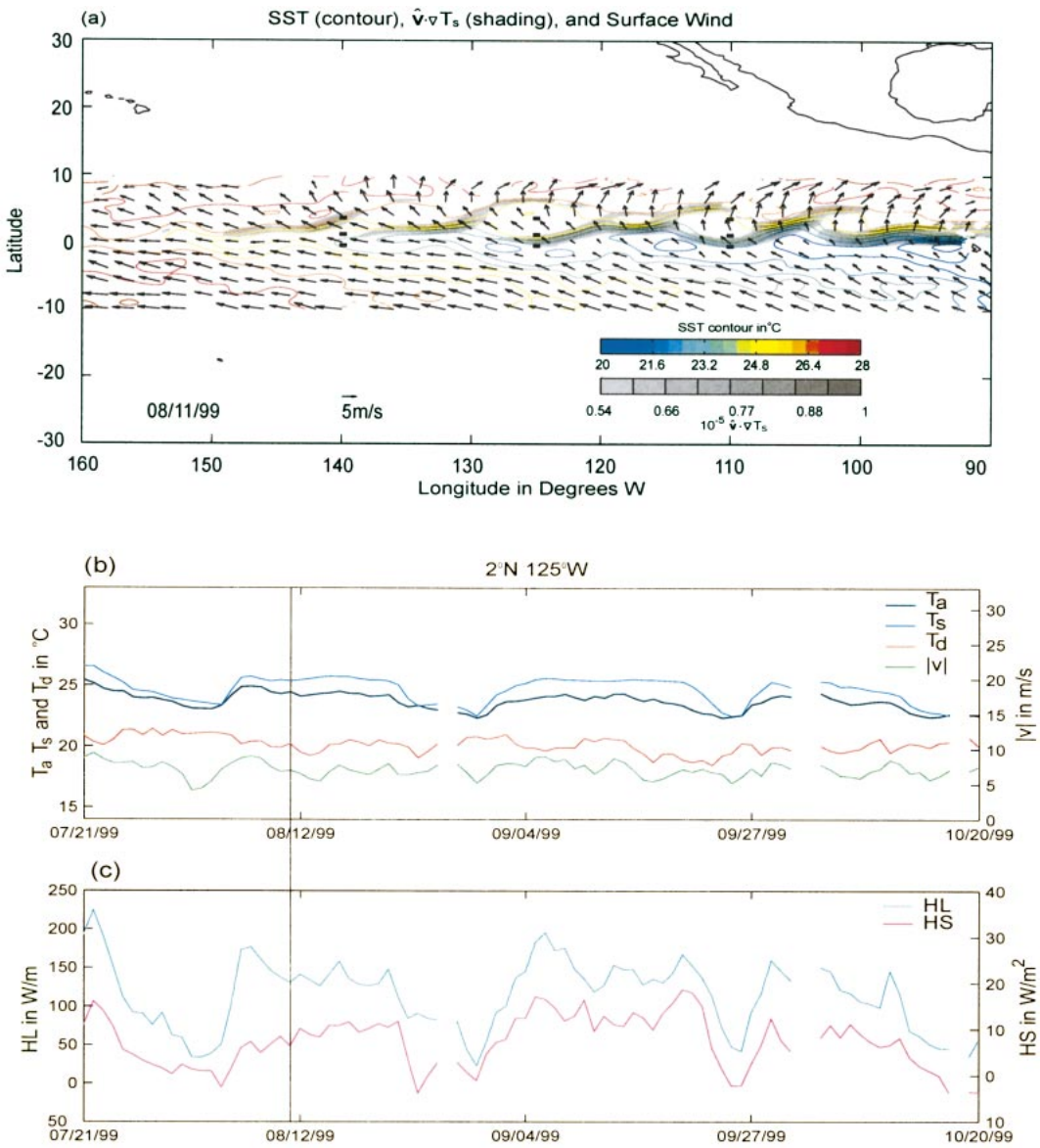

FIG. 2. (a) Three-day average map for 7–9 Aug 1999 showing TMI SST contours, QuikSCAT wind vectors, the downwind component of ∇T_S (shaded), and TAO buoy locations (squares); (b) time series of daily average air, sea, and dewpoint temperatures and wind speed magnitude from the TAO mooring at 2°N, 125°W; and (c) time series of corresponding sensible and latent heat fluxes. The vertical line in (b) and (c) indicates the corresponding date of the map shown in (a).

ary layer processes in the region of interest (Figs. 2b,c). Sensible and latent heat fluxes are inhibited during periods when the mooring is located in the relatively cool water of the TIW cusps. A sharp increase in SST indicates the passage of the TIW-induced SST front where sensible and latent heat fluxes increase rapidly. During the warm phase with relatively high SST, the fluxes of sensible and latent heat remain high but decrease rapidly with the passage of the cold front of the TIW-induced SST wave. It is apparent that the regimes over the cold and warm water are significantly different and that the ABL response to the TIW disturbances is crucial to understanding the boundary layer physics of the region. Time series from the sparse distribution of the TAO moorings do not resolve the spatial structure of TIWs. To interpret the buoy time series in the context of the propagating TIWs, it is necessary to transform the continuous temporal information of the mooring time series to more relevant spatial and phase information related to the propagating TIWs with the help of satellite data. The simultaneous usage of satellite and in situ measurements and the transformation from time to space/phase allows the interpretation of sparse buoy data with respect to the propagating TIW signals. This interchange

of time and space is described section 3a, and the transformation from time to phase is discussed in section 3b.

We study the ABL response using two different compositing methods—Lagrangian compositing along trajectories and Eulerian compositing relative to the TIW phase. For the Lagrangian trajectory method, the ABL response is investigated following an idealized ABL air column propagating across the northern equatorial SST front from cold to warm water. As the time series of meteorological variables indicate (Figs. 2b,c), the buoys at 2°N are located in a region with high SST variability of 3°–4°C associated with TIWs (see also Fig. 2 of Chelton et al. 2000). Depending on the phase of the TIW, the buoys can be located in warm or cold water or in the transitional frontal region. The wind vectors and the SST pattern can be used to construct idealized ABL trajectories and to composite sensible and latent heat fluxes and other meteorological variables depending on the measurement's location relative to the position of the SST front.

For the Eulerian wave composite, the regional ABL response to the spatial pattern of TIW-induced SST variability is of interest. From this perspective, both the SST pattern and the ABL response show a wavelike behavior. The recurring characteristics of the wavelike atmospheric response can be composited using the phase information of the waves inferred from the SST field.

a. Trajectory compositing

This compositing method transforms the independent variable ''time'' of the buoy point measurements into ''space'' using satellite maps of SST and wind. For this analysis the distance between the buoy and the SST front along an air parcel trajectory across the front is of interest (see Fig. 3). For each measurement in the buoy time series, the wind field defines trajectories connecting the buoys with the upstream front. The time required for an air parcel to cross the SST front is much shorter than the timescale of TIW change at a point in space, because the phase propagation of the TIWs is about 0.5 m s^{-1}, while the wind speed is more than 5 m s^{-1}. Each buoy location can be associated with a distance along the trajectory to the SST front. In this manner the time series are enhanced by relating the spatial information from the satellite maps to the time series.

This compositing method requires a definition of the boundaries of the frontal region from which the distance from the buoys can be measured. We chose the magnitude of the downwind component of the SST gradient; that is, $\hat{\mathbf{v}} \cdot \nabla T_S$, where $\hat{\mathbf{v}}$ is the dimensionless unit wind vector and T_S the SST, to identify the region of potentially strong air–sea interaction along the SST front. Areas where $\hat{\mathbf{v}} \cdot \nabla T_S$ exceeds 5.4×10^{-6} K m^{-1} is considered as part of the frontal region with frontal boundaries of $\hat{\mathbf{v}} \cdot \nabla T_S = 5.4 \times 10^{-6}$ K m^{-1}.

The quantity $\hat{\mathbf{v}} \cdot \nabla T_S$ was calculated from QuikSCAT vector wind and TMI SST. The 3-day mean QuikSCAT wind field defines the idealized trajectory and it determines whether the front is located in the upstream or downstream direction from the mooring location. The trajectory containing the buoy location for a given 3-day period intersects the frontal region at both the warm and the cold side of the front. Each buoy observation in the time series was assigned a distance to an SST frontal boundary along the trajectory (see Fig. 3). For rare cases when both an upstream and a downstream frontal region were present, only the upstream frontal region was chosen. To account for different widths and to avoid smearing the edges of the frontal region, *two* distances were measured: 1) the distance to the warm side and 2) the distance to the cold side of the front. Distances were either taken positive for measurements in the upstream direction or negative in the downstream wind direction. The data are divided into three regions: 1) upstream from the front, 2) within the front, and 3) downstream of the front. For the first and last case, the data are binned as a function of the distance in km to the closest frontal boundary (i.e., the warm side in region 1 and the cold side in region 3). For the second region where the buoy is located within the front, the distance to either side is normalized by the width of the front (280 km on average) and is interpolated in relative units (see Fig. 6). The results of this method are presented in section 4a.

b. Wave compositing

The spatial structure of the SST field in the satellite maps provides information about the phase of the TIWs. We use complex empirical orthogonal functions (CEOFs) to provide an objective means of determining the phase of TIW SST anomalies (Barnett 1983). The CEOF analysis allows a phase angle to be assigned to each TAO measurement time. Compositing is then performed by averaging TAO measurements having similar phase angles. The resulting dataset provides boundary layer measurements as a function of TIW phase angle. By using the wave phase angle at 2°N as a reference, the structure that is coherent with the strongest TIW activities at 2°N is revealed by compositing buoy and satellite measurements at all latitudes to obtain phase–latitude maps. These maps can be used to infer the spatial and temporal response of the ABL to TIW disturbances (Fig. 7).

The CEOF analysis is an extension of classic EOF analysis to describe traveling wave patterns in a single complex mode (Horel 1984). In this analysis, the original times series at each location x_m is augmented by the Hilbert transform to form a complex analytical signal. For practical considerations, the Hilbert transform is approximated by a discrete convolution

$$\hat{y}_H(t_n) = \sum_{m=-M}^{M} y(t_n - m\Delta t)\hat{h}(m\Delta t), \qquad (1)$$

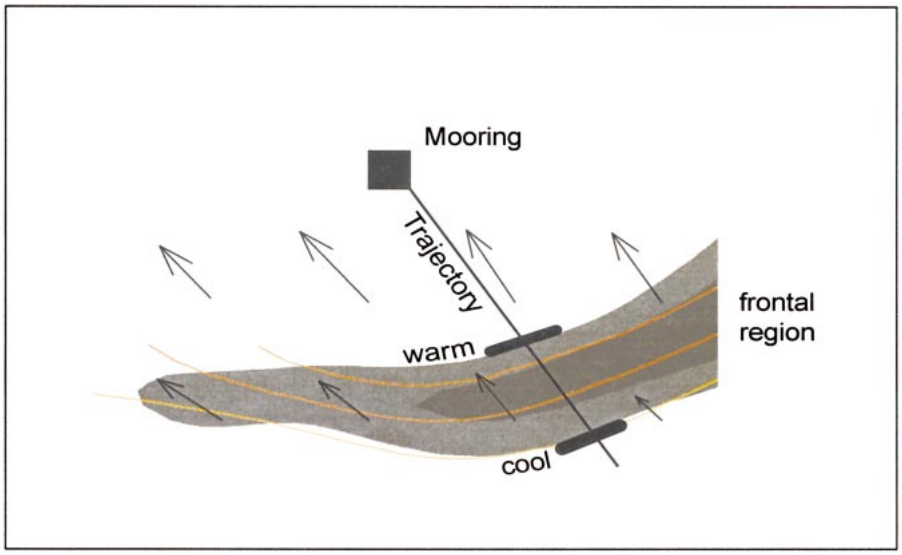

FIG. 3. Schematic relationship of the TAO mooring position to the SST front when the mooring is located downstream from the front. QuikSCAT wind vectors are indicated.

where Δt is the discrete sample interval, $M\Delta t$ is the half span of the convolution filter, and $\hat{h}(m\Delta t)$ is the filter. Oppenheimer and Schafer (1975) suggest the simple but adequate filter function

$$\hat{h}(m\Delta t) = \begin{cases} \dfrac{2}{\pi m}\sin^2(\pi m\Delta t/2) & \text{if } m \neq 0 \\ 0 & \text{if } m = 0, \end{cases} \tag{2}$$

which provides the desired properties of approximate unit amplitude response and $\pi/2$ phase shift. To reduce the effect of ''ripples'' in the Hilbert transform within $M\Delta t$ of the edges of the data record, M is commonly restricted to relatively small values (in this analysis $M = 7$) and data values within $M\Delta t$ of the beginning and end of the data record are eliminated.

The CEOF expansion in terms of amplitude and phase is

$$z(x_m, t) = \sum_{k=1}^{K} A_k^a(t)e^{i\phi_k^a(t)}A_k^F(x_m)e^{i\phi_k^F(x_m)}, \tag{3}$$

where

$$A_k^F(x_m) = [F_k^*(x_m)F_k(x_m)]^{1/2} \tag{4}$$

$$\phi_k^F(x_m) = \tan^{-1}\left\{\frac{\mathrm{Im}[F_k(x_m)]}{\mathrm{Re}[F_k(x_m)]}\right\} \tag{5}$$

$$A_k^a(t) = [a_k^*(t)a_k(t)]^{1/2} \tag{6}$$

$$\phi_k^a(t) = \tan^{-1}\left\{\frac{\mathrm{Im}[a_k(t)]}{\mathrm{Re}[a_k(t)]}\right\}. \tag{7}$$

During the period of interest, the pattern of propagating disturbances associated with TIWs is well represented by the first CEOF mode. The analysis provides the spatial phase $\phi_1^F(x_m)$ and temporal phase $\phi_1^a(t)$ for this mode that can be used to calculate phase speed estimates in the time–longitude domain

$$c_p(x_m, t) = \frac{d\phi_1^a(t)/dt}{d\phi_1^F(x_m)/dx}, \tag{8}$$

where ϕ_1^F is the spatial phase of the first CEOF mode calculated from TMI SST data along the 2°N parallel from 0° to 6° latitude and from 90° to 160° longitude. These phase speed estimates, when overlaid on the Hovmöller diagram of SST anomalies (Figs. 4, 5), define the phase propagation. Any chosen phase angle at the beginning of the data record or along a longitude near 100°W, that is, the lower and right-hand sides in Figs. 4 and 5, can be traced throughout the Hovmöller diagram along contours of constant phase angle. As shown in Figs. 4 and 5b, these phase lines for the first CEOF mode follow very closely the TIW propagation in the full anomaly field constructed from TMI SST. The SST anomalies in the reconstructed SST field from mode 1 (Figs. 4, 5c) are clearly an important part of the total TIW SST variability. This mode explains 26% and 23% of the total variance for the first and second TIW season, respectively. Inferring the phase state of the wave from the mode-1 CEOF, the TAO mooring time series can be resampled as a function of phase angle (see section 4b).

c. Heat flux calculations

The version 2.6 Coupled Ocean–Atmosphere Response Experiment (COARE) algorithm (Grachev and Fairall 1997; Grachev et al. 2000) was applied to the TAO in situ measurements to calculate the sensible and latent heat fluxes for the periods from 28 July 1999 to 27 January 2000 and 28 June 2000 to 27 January 2001.

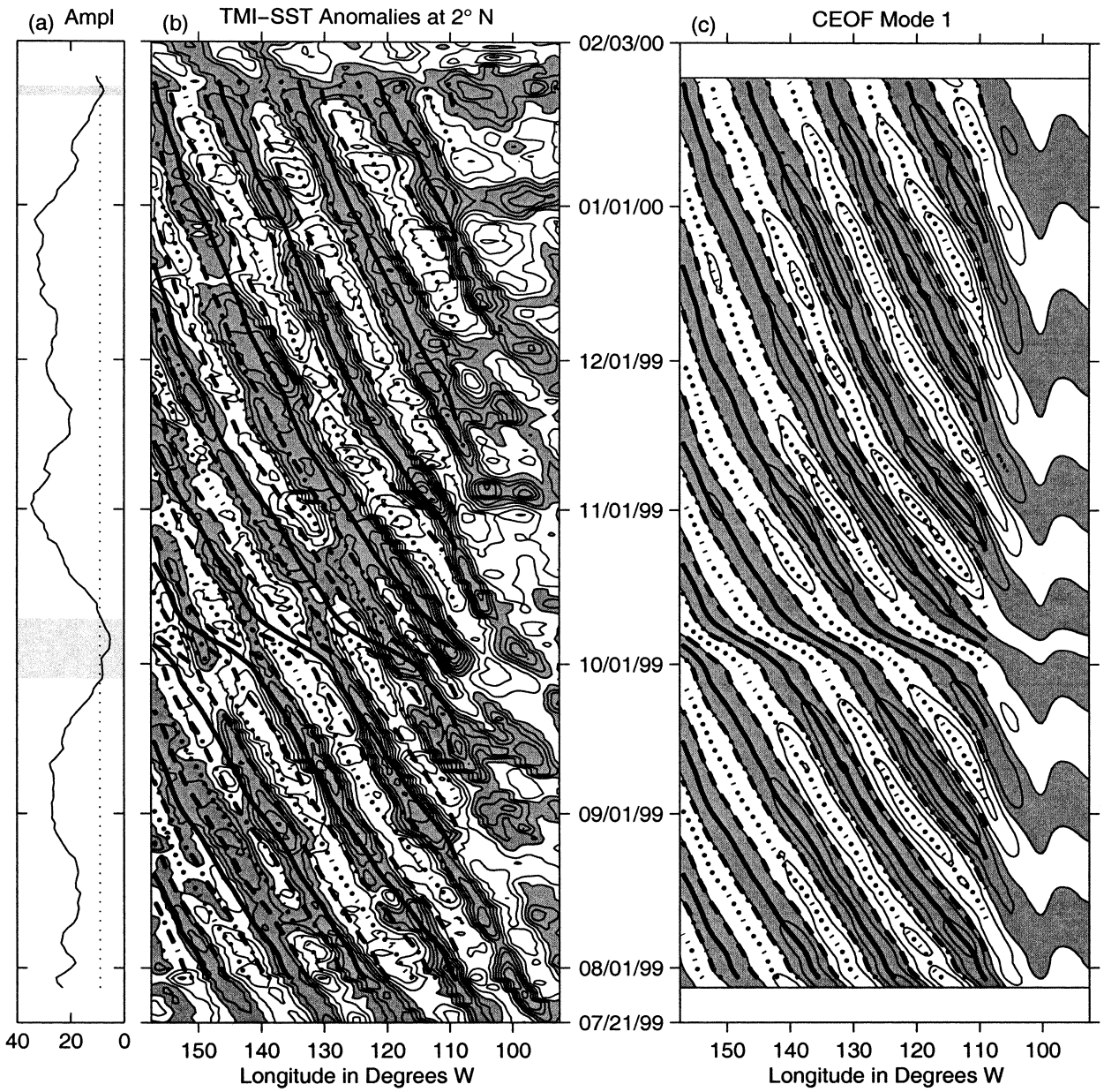

FIG. 4. 1999–2000 TIW season: (a) mode-1 CEOF amplitude time series with amplitudes smaller than the cutoff value shaded; (b) Hovmöller (time–lon) diagram of TMI SST anomalies at 2°N; and (c) Hovmöller diagram of reconstructed mode-1 SST anomalies at 2°N. In (b) and (c), the gray shaded areas correspond to negative anomalies; white areas to positive anomalies. Contour interval is 0.5°C. The phase lines superimposed on (b) and (c) represent 0° (black), 90° (dashed), 180° (dotted), and 270° (dash–dotted) phase angle from the dominant CEOF shown in (c).

The cool skin effect was included, but not the subsurface warm layer physics (Fairall et al. 1996) since the lack of radiation and precipitation measurements makes the calculation of warm layer effects a practical impossibility. We believe, however, that the potential underestimation of the fluxes in the TIW region due to lack of warm layer effects is relatively small and that inclusion of this effect would not significantly alter the conclusion of this study. In the low wind stress region over the cold tongue, precipitation is light and the solar energy is probably distributed over a relatively thick oceanic layer and would therefore have little incremental effect on the warm layer temperature and SST. Over the warm water, strong wind acts to distribute any accumulation of heat through enhanced vertical mixing of near-surface water with deeper water and tends to destroy the warm surface layer. Weak wind stress is found only in the weakly stable boundary layer regime over the cold water. The wind stress increases rapidly across the SST front.

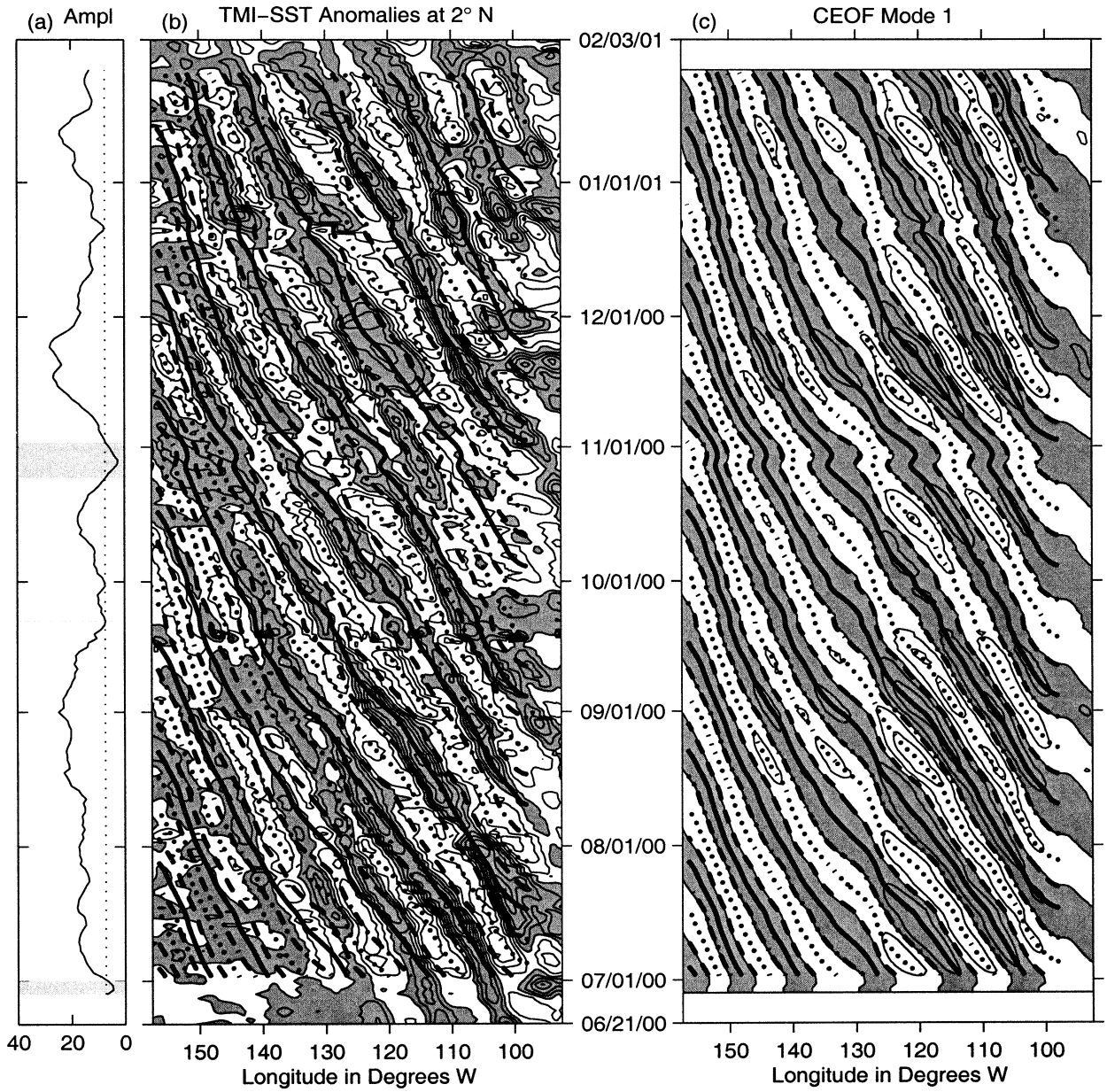

FIG. 5. Same as Fig. 4 for the 2000–2001 TIW season.

The error in the heat fluxes due to the neglect of warm layer effects is estimated by heat flux calculation at 0°, 110°W where a 90-day data record of shortwave radiation is available. The sensible heat flux was found to be underestimated by less than 0.5 W m^{-2}, while the root-mean-square error in latent heat flux was about 1.2 W m^{-2} when the shortwave radiation was omitted. These values represent 3.3% and 1.0% of the total change of 15 and 120 W m^{-2} of sensible and latent heat fluxes across the front, respectively.

The longwave radiation flux needed for the cool skin calculation was obtained using the bulk formula of Berliand and Berliand (1952). This approximation is a simple balance between an estimate of the upward cloud-free net loss of longwave radiation at the ocean surface determined by the air and sea temperature and the downward radiation flux due to clouds and moisture. The net flux for infrared radiation is given by

$$F_l \approx \epsilon\sigma T_a^4(p - q\sqrt{e}) + 4\epsilon\sigma T_a^3(T_s - T_a), \quad (9)$$

where T_a and T_s are the daily mean air and sea surface temperatures, e is the water vapor pressure (in hPa), ϵ is the emissivity of water (=0.97), and σ is the Stefan–Boltzmann constant. According to Berliand and Berliand (1952), the coefficients p and q are constants equal to 0.39 and 0.05, respectively. We have neglected the

effects of cloud cover in Eq. (9). The error estimates for the sensible and latent heat fluxes calculated in this analysis are insensitive to the cloud cover values used in the cool skin calculation.

4. Results

The results are presented for the two compositing methods separately. The Lagrangian trajectory compositing in section 4a describes an ABL air column as it is advected across the SST gradient. The Eulerian phase compositing in section 4b determines the regional ABL responses to SST distributions. The complementary aspects of the two compositing methods are discussed in section 5.

a. Trajectory compositing

If the wind direction does not change rapidly with height, the prevailing southeasterly winds at the surface may be used to determine the trajectory of an idealized ABL air column as it is advected from the cool to the warm side of the SST front. In this case, the graphs shown in Fig. 6 may be regarded as the near-surface meteorological conditions and heat fluxes along the ABL trajectory from southeast (cool side) to northwest (warm side). The mean standard errors for the presented properties are included in Fig. 6.

Following an ABL air column from cold to warm water across the SST gradient, it is apparent that sensible and latent heat fluxes are inhibited on the cold side of the front. The TAO measurements of SST are about 22.5°C on the cold side of the front (Fig. 6a). Sensible heat flux is slightly negative (-2 W m^{-2}) and latent heat flux is less than 50 W m^{-2} (Fig. 6b). The latent heat flux and the associated sea surface minus air specific humidity are small, while the sensible heat flux is negative corresponding to the sea surface minus air temperature differences that are slightly negative (Fig. 6c). The TAO measurements of wind speed on the cold side are $\sim$6 m s^{-1} (Fig. 6a).

Entering the frontal zone, sensible and latent heat fluxes, SST, wind speed, and sea surface minus air specific humidity, and temperature differences increase significantly. The maxima of these quantities are found on the warm side of the frontal region where the SST is about 24.5°C. The maximum of sensible heat flux is 11 W m^{-2}, whereas the latent heat flux reaches a maximum of about 120 W m^{-2} (Fig. 6b). The wind speed increases to about 7.5 m s^{-1} at the warm side of the SST front (Fig. 6a).

North of the frontal zone, over the warmer water, the responses of sensible and latent heat fluxes are remarkably different. While sensible heat flux decreases to values of about 2 W m^{-2}, latent heat flux remains at a large value of more than 110 W m^{-2} (Fig. 6b). The behaviors of the sea minus air specific humidity and temperature differences are consistent with the latent and sensible heat fluxes, respectively. The wind speed remains more or less constant at 8 m s^{-1} (Fig. 6a).

It is apparent that sensible and latent heat fluxes increase over the strong SST gradient and persistently large values of latent heat fluxes are found over the warm water north of the SST front. The increase in surface wind speed in the region of enhanced sensible and latent heat fluxes is consistent with the ABL momentum mixing hypothesis. The associated cold air advection is responsible for the location of the maxima of the heat fluxes where the SST gradient increases (Fig. 6a). The changes of sensible and latent heat fluxes along the trajectory are very similar to the changes of the sea minus air temperature and specific humidity differences, respectively (Fig. 6c).

b. Wave compositing

The spatial and temporal structure of the ABL response to TIWs can be characterized alternatively as a function of wave phase angle. As described in section 3b, the space–time phase angle at the buoy locations can be objectively determined from the CEOF analysis at all times, and the heat fluxes can be composited for measurements with similar phase angles. Although only 26% and 23% of the variance is explained by mode 1 for the first and second TIW season, respectively, Figs. 4 and 5 show that the features of the TIW amplitude and phase propagation that are most important for the compositing are captured by mode 1; higher modes primarily describe localized strengthening and weakening of the anomalies. The calculated phase lines follow the propagation of positive (dotted lines) and negative (black lines) anomalies remarkably well (Figs. 4, 5b), especially in regions where the amplitude of the CEOF time series (Figs. 4, 5a) is large (i.e., where the westward propagation is clearly defined). The phase lines are less useful in transitional states of the TIW field; for example, in the early part of October 1999 (Fig. 4b) where the mode-1 amplitude time series is small and the westward propagation is not clearly apparent (Fig. 4a). The amplitude time series can therefore be used as an indicator of how well mode-1 phase lines represent the propagation of the anomalies. We have chosen an amplitude threshold of about 30% of the maximum amplitude to identify time periods when mode 1 is representative of the TIW phase propagation and TIW amplitude. Time periods with CEOF mode-1 amplitudes smaller than this threshold (shaded in Figs. 4a, 5a) were excluded from the analysis presented below. The analysis is insensitive to the explicit choice of the threshold.

Eight phase angles have been chosen to composite sensible and latent heat flux, specific humidity and temperature time series as a function of phase state. The results are shown in Figs. 7 and 8. All time series are composited as a function of the wave phase angle at 2°N. The latitude of 2°N was chosen because the SST signature of TIW disturbances are most energetic at this

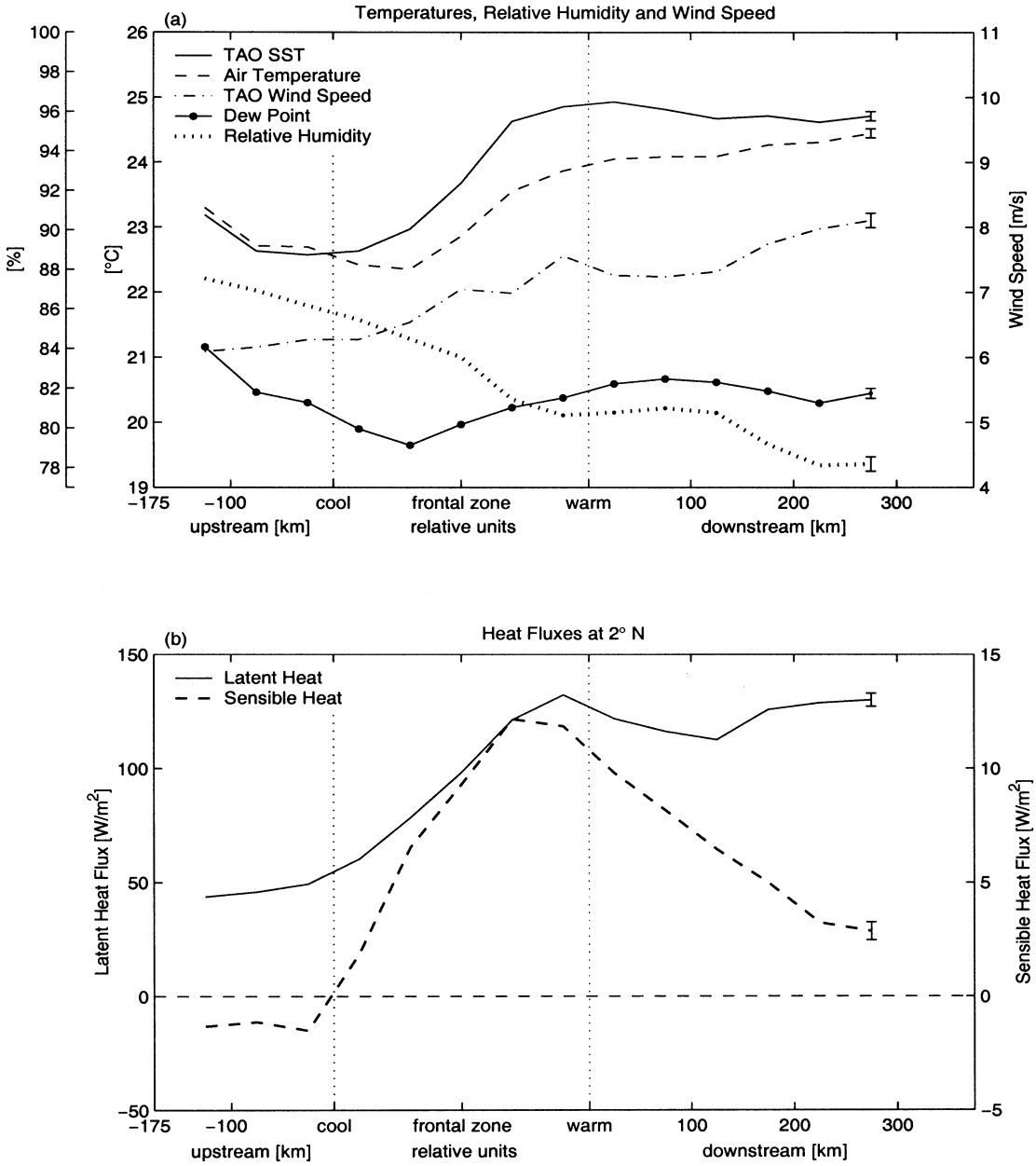

FIG. 6. (a) Binned TAO measurements of SST, air temperature, wind speed, dewpoint temperature, and relative humidity as a function of distance relative to the frontal zone; (b) same as (a) for binned latent and sensible heat fluxes; and (c) same as (a) for binned sea surface minus air temperature and sea surface minus air specific humidity. Vertical bars represent the mean of the standard errors of the binned data over the entire domain.

latitude (see Fig. 2 of Chelton et al. 2000). The interpolated and smoothed QuikSCAT wind speed and TMI SST measurements are displayed here on a 1° grid that enables the presentation of longitude–phase maps of TMI SST and wind speed (Fig. 7a), demonstrating the general characteristics of the SST and the wind patterns associated with TIWs. The longitude–phase structure of the composited TIW disturbance is shown in Fig. 7, while the presentation as line plots in Fig. 8 better reveals the magnitude and phase shift of the processes. The phase cycle is repeated twice for clarity and vertical bars represent the standard error. The eastward tilting of the cold cusps with increasing latitude can be seen in Figs. 7a and 8, which is also apparent in snapshots of SST (e.g., Fig. 1). It is apparent from the composited wind vectors (Fig. 7b) that the wind direction is not strongly affected by the SST perturbations associated with TIWs. However, the wind speed varies by ~1 m s^{-1} in response to the underlying SST field (Figs. 7a, 8) at a given latitude.

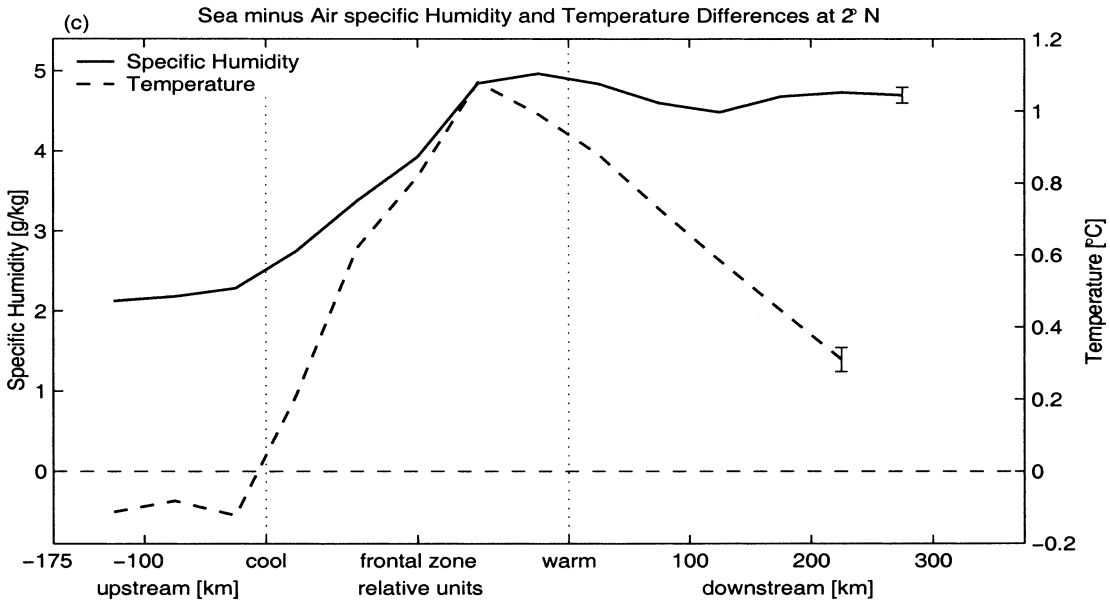

FIG. 6. (*Continued*)

A striking feature in Figs. 7b and 8a is the eastward shift of sensible heat flux at 2°N and especially at 5°N relative to the pattern of TMI SST. The eastward shift is equivalent to 38 ± 5° of wave phase (roughly equivalent to 160 km) at 2°N and 52 ± 3° of wave phase at 5°N. The phase of the patterns has been estimated by regressing a sinusoid on the composites. The uncertainty intervals are based on the 95% confidence level. The coupling of sensible heat flux to regions of strong SST gradients results in a southwest–northeast phase shift of about 85 ± 3° between the two latitudes that is associated with the tilting of the SST phase lines with increasing latitude. The relatively broad maximum of sensible heat flux at 2°N at phase angles between 180° and 270° may be related to the proximity of the front to the mooring location at all wave angles of the warm phase that would cause ABL adjustments and air–sea interactions. The maximum of sensible heat flux is located in a region of strong SST gradient at a phase angle of 225°.

The patterns of latent heat flux in Figs. 7c and 8b show an apparent eastward phase shift of 32 ± 6° of wave phase at 5°N, but only a marginal phase shift of 12 ± 7° at 2°N. At a fixed point in space along either 2° or 5°N, the latent heat flux increases rapidly toward the west in the vicinity of the SST front, from TIW phase angle 360° to 270° at 2°N and from 90° to 0° at 5°N (see Fig. 8b). However, to the west of the warmest water at 2°N, the latent heat flux decreases relatively slowly from phase angle 180° to 90°. By comparison there is a more rapid decrease toward the west at 5°N, from phase angle 270° to 180°, giving the appearance of an overall eastward phase shift of the latent heat flux pattern.

The patterns of sensible and latent heat flux are closely related to the pattern of sea minus air temperature (Fig. 7d) and sea minus air specific humidity (Fig. 7e), respectively. The humidity difference pattern is shifted to the east at 5°N, but not at 2°N, whereas the pattern of the temperature difference is clearly shifted at both latitudes with a maximum near the SST front to the east and a secondary maximum over the warmest water to the west at 2°N.

Although the sensible and latent heat flux anomalies associated with passing TIWs are primarily controlled by anomalies in the air–sea temperature and humidity differences, the use of QuikSCAT wind speeds in place of TAO wind speeds can cause small apparent phase shifts in the estimated heat flux patterns. Figure 9a shows that QuikSCAT wind speeds are shifted to the west by 38 ± 3° of wave phase at 5°N and to the east by 27 ± 10° at 2°N relative to the wind speeds observed by the TAO anemometer. There is also a mean wind speed bias (TAO minus QuikSCAT) of about 1 m s^{-1} at 2°N and 0.1 m s^{-1} at 5°N, averaged over all phase angles.

Figures 9b and 9c compare the latent and sensible heat fluxes using QuikSCAT and TAO wind speeds with all other input parameters being equal. The mean heat flux bias resembles the mean wind speed bias seen in Fig. 9a. The phase shift in the sensible heat flux pattern due to substituting QuikSCAT winds for TAO winds is not significantly different from zero. The earlier conclusion from Fig. 8 regarding the eastward shift of the sensible heat flux pattern relative to the SST pattern is therefore robust. Using QuikSCAT wind speed in place of TAO wind speed, however, reduces the eastward phase shift of latent heat flux pattern by 9 ± 6° at 5°N,

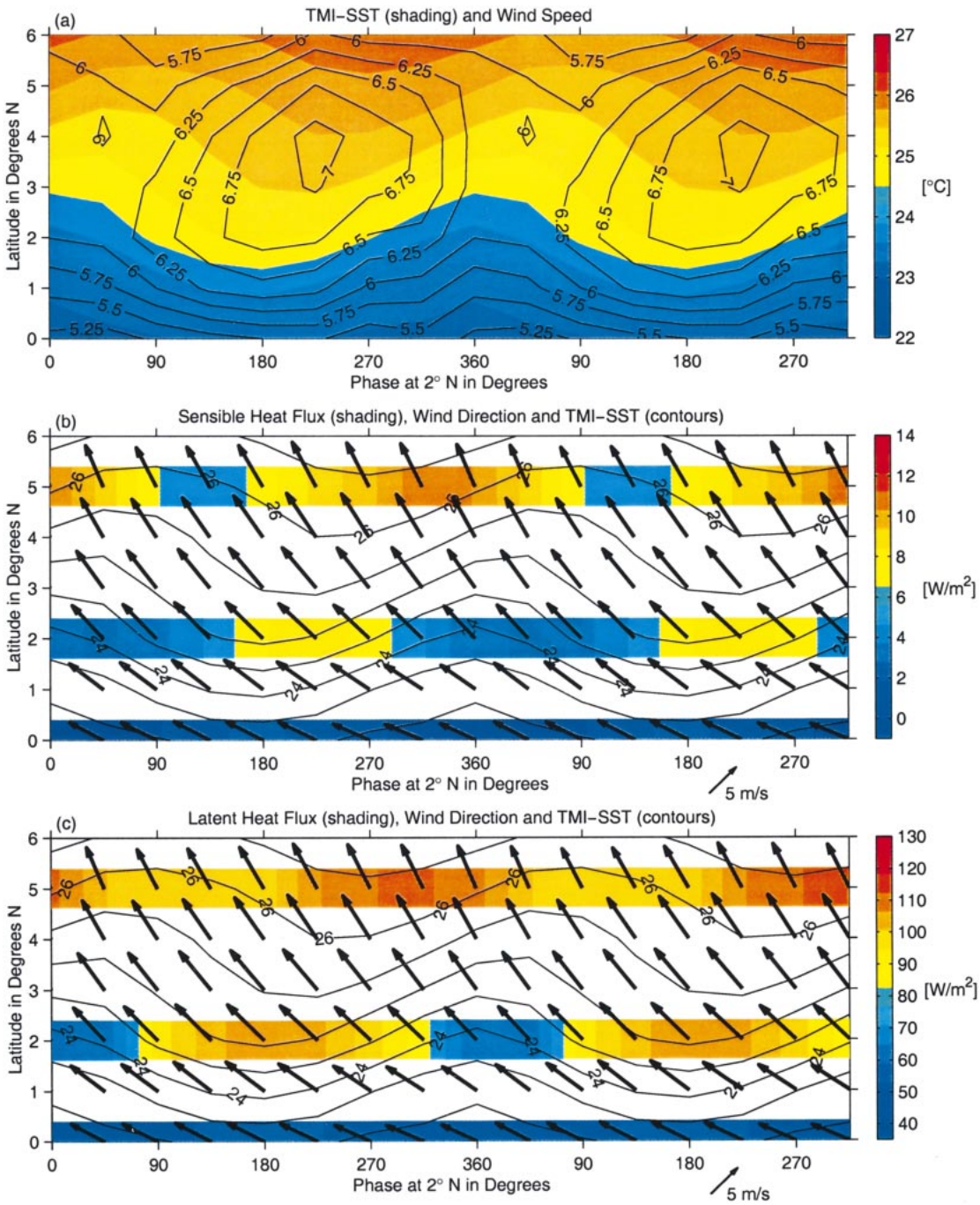

FIG. 7. Phase–latitude maps of (a) TMI SST (shading) and wind speed; (b) sensible heat flux (shading), wind direction, and TMI SST (contours); (c) latent heat flux (shading), wind direction, and TMI SST (contours); (d) sea surface minus air temperature (shading), wind direction, and TMI SST (contours); and (e) sea minus air specific humidity (shading), wind direction, and TMI SST (contours).

but increases the shift by 7 ± 9° at 2°N relative to the pattern of SST. The bias in the latent heat flux at 5°N therefore results in a smaller, but still significant, phase shift when QuikSCAT wind estimates are used for the calculations. The small eastward shift of latent heat flux at 2°N is increased by an insignificant amount.

It has been suggested that the systematic difference between the TAO and QuikSCAT wind measurements ($\mathbf{v}_T - \mathbf{v}_Q$) can be related to ocean currents (Kelly et al. 2001; Polito et al. 2001). The QuikSCAT instrument measures wind stress relative to the moving sea surface that is then converted into an equivalent 10-m neutral

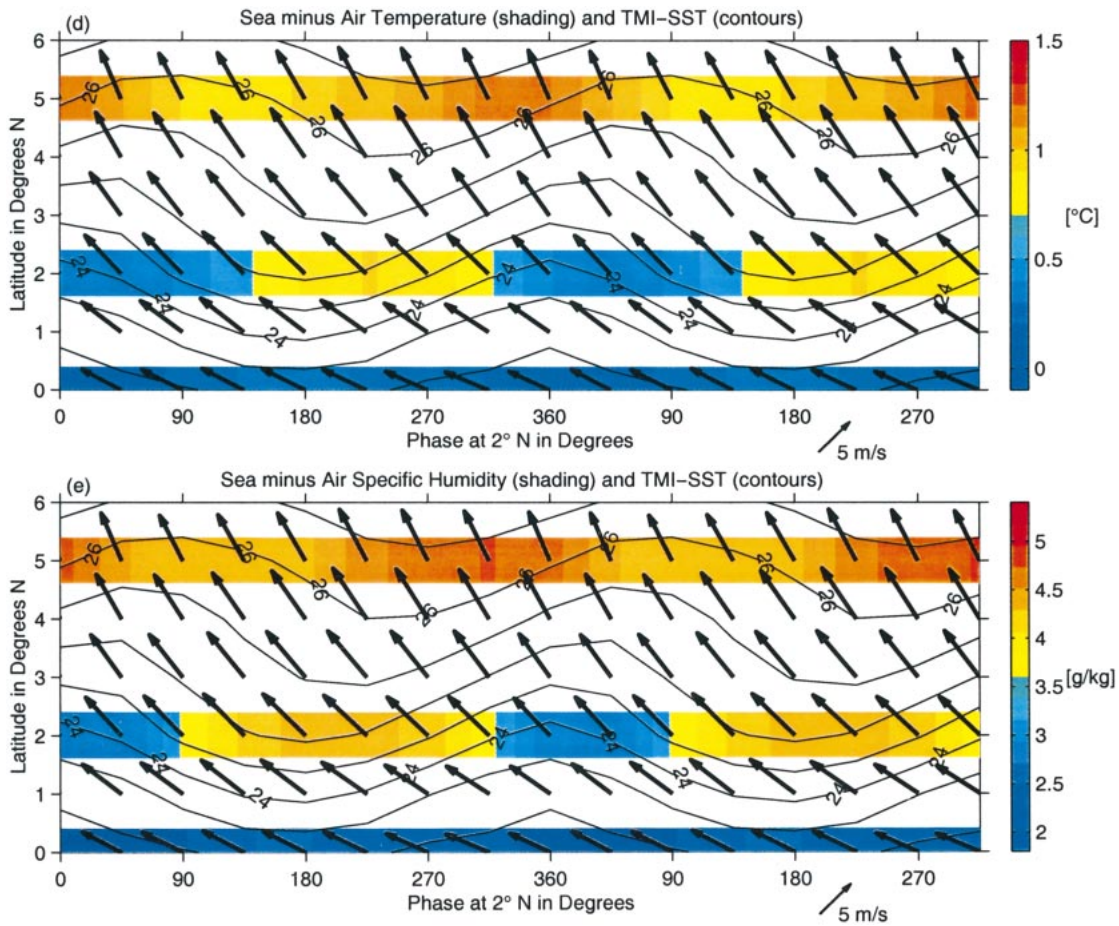

FIG. 7. (*Continued*)

wind relative to the moving surface. The TAO anemometer, on the other hand, provides a wind estimate relative to a fixed location. Wind estimates from QuikSCAT and TAO would therefore differ even if there were no observational error or differences in sampling patterns, and the difference would be related to the surface current. Note that wind speed measurements relative to the moving sea surface (e.g., stability corrected QuikSCAT winds) can be used directly for estimation of latent and sensible heat fluxes, while wind speeds relative to a fixed point (e.g., TAO winds) may require adjustment in regions with strong surface currents.

The difference between TAO and QuikSCAT winds ($\mathbf{v}_T - \mathbf{v}_Q$) also includes observational errors. Under the conditions of relatively steady wind direction and wind speed, the true mean wind plus the observational bias can be removed to obtain approximate values of the perturbation currents ($\mathbf{v}'_T - \mathbf{v}'_Q$). The analysis technique of compositing multiple TIW events thus offers the possibility of testing the hypotheses of Kelly et al. (2001) and Polito et al. (2001) by obtaining perturbation ocean current estimates averaged over a large number of TIW realizations.

The systematic nature of the composited $\mathbf{v}'_T - \mathbf{v}'_Q$ becomes apparent when overlaid on the SST composite (Fig. 9d). The inferred oceanic currents at 2°N show a cyclonic (counterclockwise) rotation and a magnitude of about 0.2 m s^{-1}. The magnitude of the derived currents at 5°N is smaller, on the order of 0.1 m s^{-1}, with anticyclonic (clockwise) rotation of the perturbation vector. For a given phase angle, the latitude of the observation relative to the center of the perturbing eddy determines the direction of the current vector rotation with TIW phase. The zonal component of the current perturbation north of the eddy circulation center is opposite the zonal component of the perturbation south of the center. The sense of the rotation in Fig. 9 suggests that the location at 2°N is mostly south and that 5°N is mostly north of the center of the perturbing eddy. Relatively cold SST is advected northward and warm SST southward at 2°N. The relationship between inferred currents and SST is not as systematic at 5°N, and the magnitude of inferred currents and SST anomalies are much smaller. The relationship between composited SST and the inferred currents is consistent with the observational study of Kennan and Flament (2000) who investigated a TIW vortex during the fall of 1990 from numerous observation platforms. The results of our

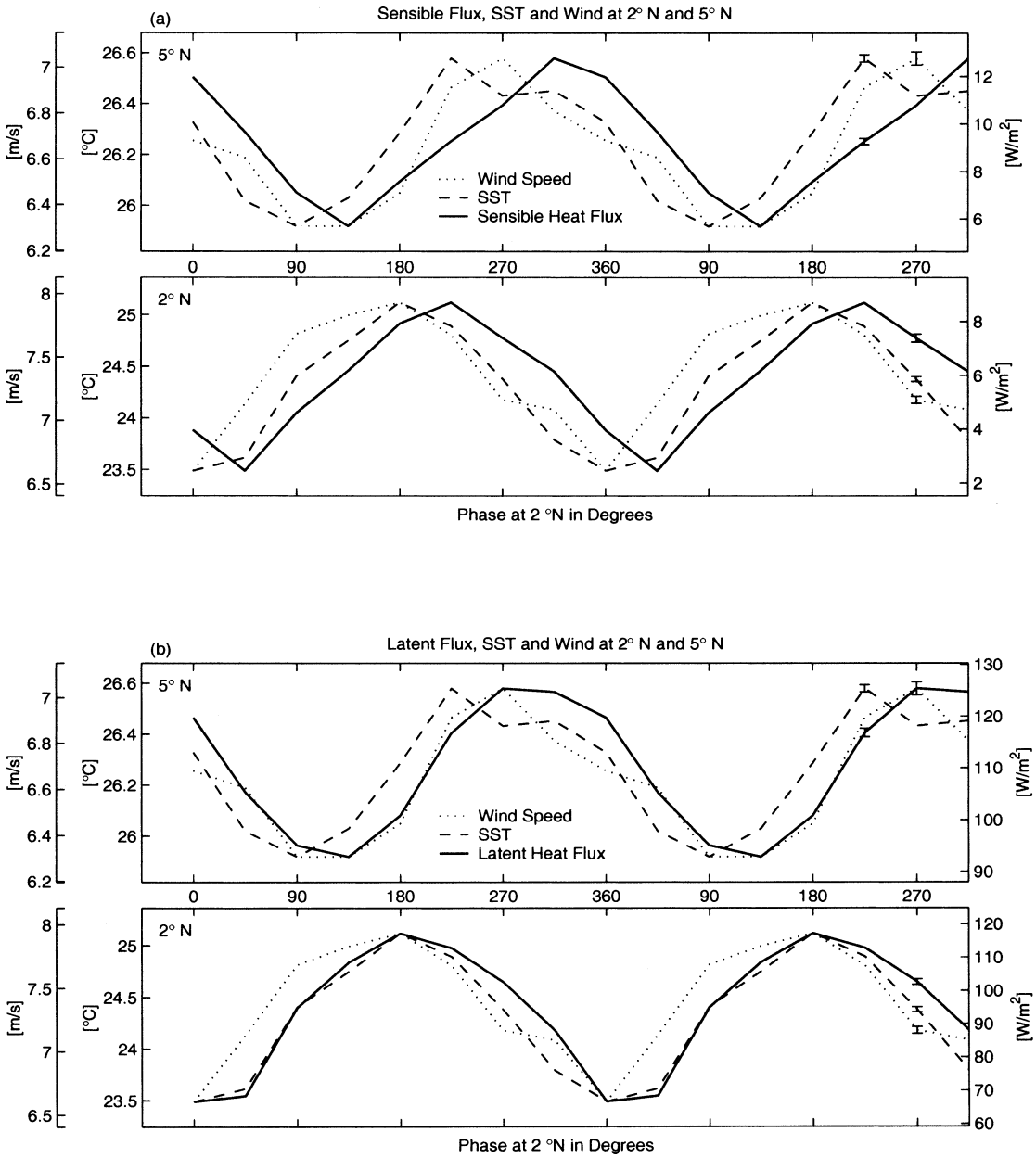

FIG. 8. (a) Sensible heat flux, SST, and wind speed (top) at 5°N, (bottom) at 2°N. (b) Latent heat flux, SST, and wind speed (top) at 5°N, (bottom) at 2°N. Vertical bars represent the mean of the standard errors for the binned data over the entire domain.

study suggest that the center of the TIW circulations were located just south of 5°N and the northward eddy heat flux due to the composite TIW disturbance was larger at 2°N than at 5°N.

Along with the estimated perturbation currents, geostrophic surface currents derived from TOPEX sea surface height (SSH) fields are overlaid in Fig. 9. Because of the dependence of the geostrophic currents on the inverse Coriolis parameter, it was necessary to spatially smooth the SSH fields to suppress the effects of measurement noise in the velocity fields estimated from SSH. In addition, the 10-day sampling pattern of the TOPEX orbit required temporal smoothing of the data. The loess filter applied here (Greenslade et al. 1997) has a filter transfer function that is essentially equivalent to that of 4° of longitude by 1° of latitude by 15-day block averages. The half-power filter cutoffs are at about 8° of longitude by 2° of latitude by 30 days. This spatial and temporal smoothing is comparable to the 1200-km wavelength and 30-day periodicity of TIWs (Qiao and Weisburg 1995). It can therefore be anticipated that the velocities inferred from the filtered TOPEX data will

be somewhat attenuated. This indeed appears to be the case. The magnitude of the current estimates using TOPEX SSH fields are about a factor of 4 smaller than the inferred currents from the wind measurements. For displaying purposes, the scale of the TOPEX estimates in Fig. 9d has therefore been enhanced to compensate for the reduction from the filtering. The direction of the geostrophic currents is not altered significantly by the smoothing and is reasonably consistent with the derived currents from the wind analysis, except in regions where the wind is blowing normal to the front from cold to warm SST. The consistency between the independently estimated geostrophic current perturbations from TOPEX and the current estimates from TAO minus QuikSCAT winds support the hypothesis that oceanic currents are responsible for the differences between QuikSCAT and TAO perturbation wind measurements.

The mean difference between QuikSCAT and TAO winds ($\overline{\mathbf{v}}_T - \overline{\mathbf{v}}_Q$), however, is more difficult to interpret. It is plausible that the mean zonal component of the difference between TAO and QuikSCAT ($\overline{u}_T - \overline{u}_Q$) is due to a westward oceanic current as Kelly et al. (2001) suggest. It remains unclear, however, why the mean meridional component ($\overline{v}_T - \overline{v}_Q$) is large and negative in a region of mean zonal equatorial surface currents. Observational biases in QuikSCAT or TAO might be responsible, at least in part, for the difference in both the zonal and meridional components of $\overline{\mathbf{v}}_T - \overline{\mathbf{v}}_Q$.

5. Discussion and conclusions

The two compositing methods presented in this study allow a detailed description of near-surface boundary layer conditions across the perturbed SST front. It has been shown that the boundary layer response to oceanic forcing by the SST is shifted eastward relative to the pattern of SST. The spatial shift is larger at 5° than at 2°N. The enhancement of sensible heat flux across the front is a much larger fraction of its background values on either side of the front than is the enhancement of latent heat flux. On the larger scale, relatively warm water in TIW disturbances is associated with relatively large sensible and latent heat fluxes. Over relatively cool water, the fluxes are smaller. However, temperature advection appears to have an important effect on the ABL heat budget, shifting the sensible heat flux pattern toward the east relative to the SST anomalies.

Sweet et al. (1981) hypothesized that the acceleration of boundary layer air across an SST front can be caused by enhanced downward mixing of momentum in the unstable boundary layer regime. Hayes et al. (1989) proposed this mechanism to explain the observed wind patterns in association with TIW-induced SST perturbations. The enhanced momentum mixing is expected to be accompanied by increased sensible and latent heat fluxes. The boundary layer would be expected to be out of equilibrium when the change of temperature at the surface is rapid. The adjustment timescale may be larger downstream from the frontal zone than within the frontal zone and the ABL properties may adjust more slowly to the equilibrium values.

By combining the results of the two compositing methods, a detailed picture of air–sea interaction can be obtained in terms of magnitude and distribution of surface sensible and latent heat flux responses to TIWs. It is clear that the atmospheric response provides a negative feedback to the TIW SST anomalies in this region. Latent and sensible heat fluxes tend to cool the positive and warm the negative SST anomalies. The latent heat flux anomalies of about 40 W m^{-2} are the primary contributor to the cooling/warming of the SST anomalies. This is consistent with the estimate of 50 W m^{-2} (1 K)$^{-1}$ change obtained by Zhang and McPhaden (1995) from a much more limited dataset. Distributing the 40 W m^{-2} latent heat flux over a layer of about 50-m depth yields an instantaneous heating rate of 1.6×10^{-2} K day^{-1}. For a typical TIW periodicity of 30 days, the temperature change due to latent heat flux would be about 0.5°C. In addition, the enhanced vertical mixing over the warmer water generates increased low-level cloudiness that reduces the solar insolation that reaches the sea surface (Deser et al. 1993). If the compensating longwave effect of the clouds is taken into account, the cooling effect from the increased cloudiness may be as large as ~0.6°C (month)$^{-1}$ (Deser et al. 1993).

The patterns of latent heat flux associated with TIWs show an apparent eastward phase shift at 5°, but not at 2°N. The wave composites do not contain enough information to draw firm conclusions about the reasons for these differences. It is plausible, however, that the lack of a phase shift at 2°N may be due to the relatively close proximity of the SST front. The controls on boundary layer humidity appear to be different than the controls on temperature. Figure 6 suggests that more time is required to modify the boundary layer humidity structure than the temperature structure. The air temperature in Fig. 6a appears to follow the SST with a relatively short time lag along the air parcel trajectory, while the dewpoint changes more slowly across the SST front and is relatively constant downwind over the warm water. Friehe et al. (1991) note such an apparent difference of the adjustment times of the humidity and temperature field during the Frontal Air–Sea Interaction Experiment (FASINEX) in the western North Atlantic. In addition the driest boundary layer air appears to be located within the frontal zone (see Fig. 6a). Therefore, the specific humidity in the frontal region just to the north of the cold tongue, where the air is blowing more or less parallel to the SST front, may be relatively dry and affected little by upstream air–sea interaction across the frontal boundary. These factors may result in the relatively slow westward decrease of the composited air–sea humidity difference and the latent heat flux in the 2°N wave composite. Additional observations above the atmospheric surface layer would be useful for exploring this hypothesis.

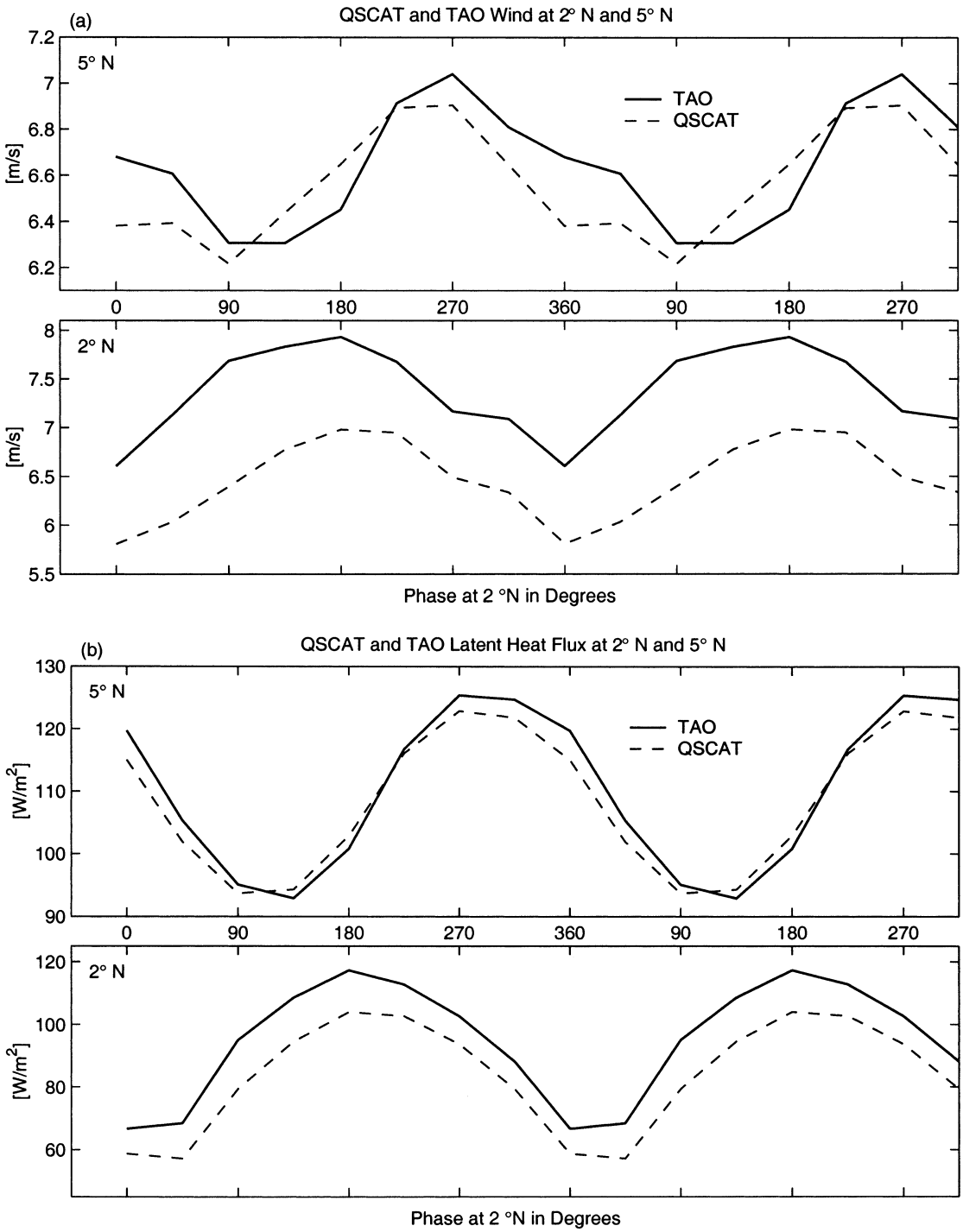

FIG. 9. (a) QuikSCAT and TAO wind speed (top) at 5°N, (bottom) at 2°N; (b) same as (a) for QuikSCAT and TAO latent heat flux; (c) same as (a) for QuikSCAT and TAO sensible heat flux; (d) same as (a) for estimated ocean current perturbations from QuikSCAT and TAO winds ($\mathbf{v}'_T - \mathbf{v}'_Q$) and TOPEX geostrophic surface current estimates.

As expected, ocean surface currents provide a physically consistent explanation for the differences observed between QuikSCAT and TAO wind anomalies in our TIW composites. The differences in wind speed enter the heat flux calculation through the dependence of the fluxes on wind speed, but do not significantly alter the conclusions regarding the relationship of sensible and latent heat flux anomalies to the TIW SST pattern.

The results of the heat flux analysis obtained here are consistent with the ABL momentum mixing hypothesis

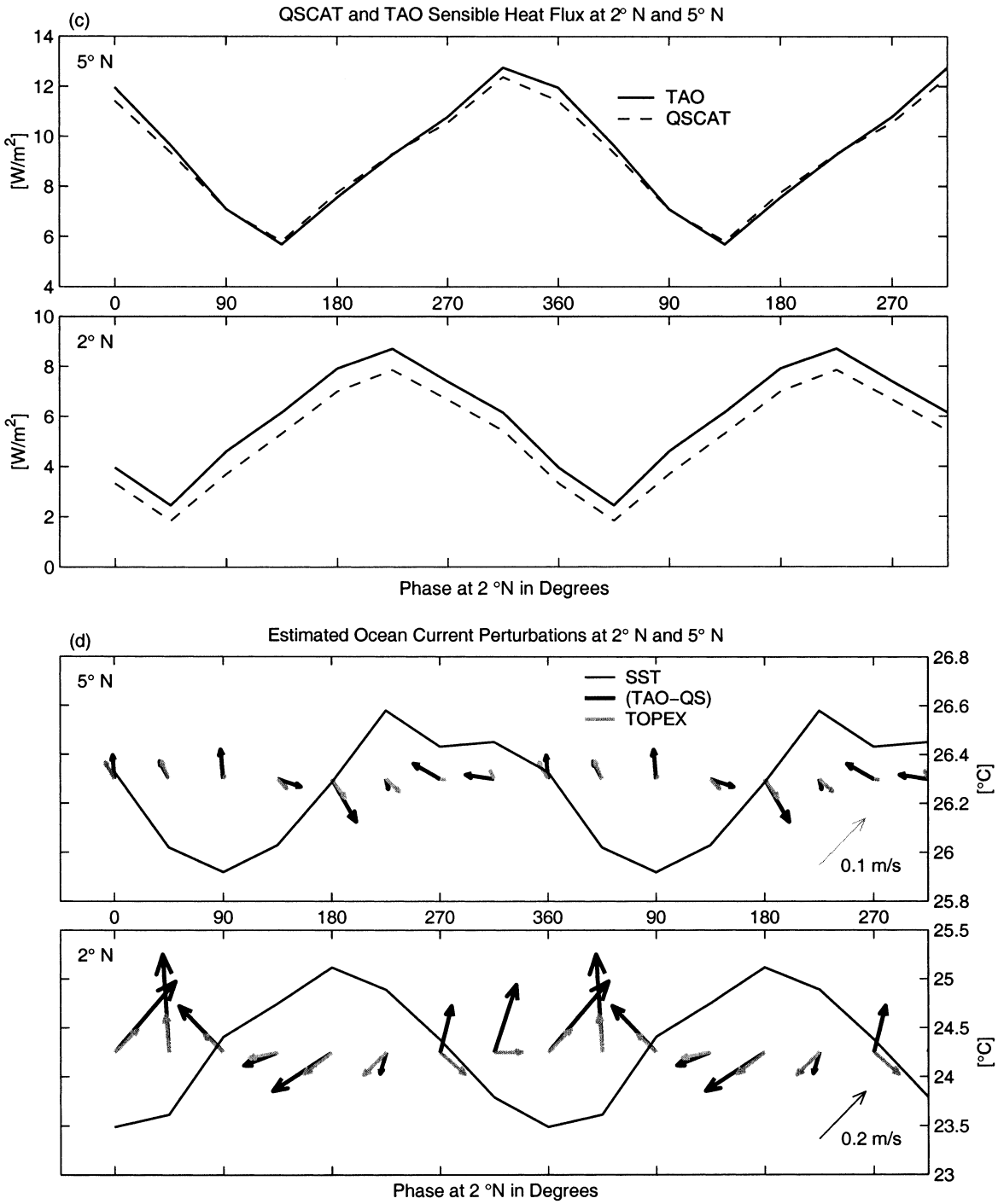

FIG. 9. (*Continued*)

and can be seen as complementing the results of Wallace et al. (1989) and Chelton et al. (2001). Air–sea interaction appears to explain both the wind pattern and the patterns of sensible and latent heat fluxes relative to the SST front. Based on surface observations alone, however, it is not possible to infer with certainty that the increase in the speed of the low-level wind is due solely to ABL momentum mixing. It is possible that a low-level pressure adjustment (Hashizume et al. 2002; Wai and Stage 1989; Lindzen and Nigam 1987) may also be important. Future observational and modeling work will need to focus on investigation of the vertical structure of the boundary layer to distinguish between the various mechanisms.

Acknowledgments. We would like to thank Shang-Ping Xie and Mike Freilich for helpful discussions and suggestions, and thank the reviewers for constructive comments and suggestions. We gratefully acknowledge Michael Schlax for providing the gridded TMI, QuikSCAT, and TOPEX fields and a number of helpful discussions. The research presented in this paper was supported by NOAA Grant NA96GP0368 from the Office of Global Programs and NASA Grant NAS532965 for funding of Ocean Vector Winds Science Team activities. MJM acknowledges support of NOAA's Office of Oceanic and Atmospheric Research.

REFERENCES

Barnett, T. P., 1983: Interaction of the monsoon and Pacific trade wind system at interannual time scales. Part I: The equatorial zone. *Mon. Wea. Rev.,* **111,** 756–773.

Berliand, M. E., and T. G. Berliand, 1952: Determining the net long-wave radiation of the Earth with consideration of the effect of cloudiness. *Izv. Akad. Nauk SSSR, Ser. Geofiz,* **1,** 64–78.

Bond, N. A., 1992: Observations of planetary boundary-layer structure in the eastern equatorial Pacific. *J. Climate,* **5,** 699–706.

Chelton, D. B., F. J. Wentz, C. L. Gentemann, R. A. de Szoeke, and M. G. Schlax, 2000: Microwave SST observations of trans-equatorial instability waves. *Geophys. Res. Lett.,* **27,** 1239–1242.

——, M. G. Schlax, S. K. Esbensen, N. Thum, M. H. Freilich, F. J. Wentz, C. L. Gentemann, and M. J. McPhaden, 2001: Observations of coupling between surface wind stress and sea surface temperature in the eastern tropical Pacific. *J. Climate,* **14,** 1479–1498.

Deser, C., J. J. Bates, and S. Wahl, 1993: The influence of sea surface temperature gradients on stratiform cloudiness along the equatorial front in the Pacific Ocean. *J. Climate,* **6,** 1172–1180.

Fairall, C. W., E. F. Bradley, J. S. Godfrey, G. A. Wick, J. B. Edson, and G. S. Young, 1996: Cool-skin and warm-layer effects on sea surface temperature. *J. Geophys. Res.,* **101,** 1295–1308.

Freilich, M. H., cited 1996: SeaWinds algorithm theoretical basis document. [Available online at http://eospso.gsfc.nasa.gov/atbd/seawindstables.html.]

Friehe, C. A., and Coauthors, 1991: Air–sea fluxes and surface layer turbulence around a sea surface temperature front. *J. Geophys. Res.,* **96,** 8593–8609.

Grachev, A. A., and C. W. Fairall, 1997: Dependence of the Monin–Obukhov stability parameter on the bulk Richardson number over the ocean. *J. Appl. Meteor.,* **36,** 406–414.

——, ——, and E. F. Bradley, 2000: Connective profile constants revisited. *Bound.-Layer Meteor.,* **3,** 495–515.

Greenslade, D. J. M., D. B. Chelton, and M. G. Schlax, 1997: The midlatitude resolution capability of sea level fields constructed from single and multiple satellite altimeter datasets. *J. Atmos. Oceanic Technol.,* **14,** 849–870.

Hashizume, H., S. P. Xie, M. Fujiwara, M. Shiotani, T. Watanabe, Y. Tanimoto, W. T. Liu, and K. Takeuchi, 2002: Direct observations of atmospheric boundary layer response to SST variations associated with tropical instability waves over the eastern equatorial Pacific. *J. Climate,* **15,** 3379–3393.

Hayes, S. P., M. J. McPhaden, and J. M. Wallace, 1989: The influence of sea-surface temperature on surface wind in the eastern equatorial Pacific. Weekly to monthly variability. *J. Climate,* **2,** 1500–1506.

Horel, J. D., 1984: Complex principal component analysis: Theory and examples. *J. Climate Appl. Meteor.,* **23,** 1660–1673.

Kelly, K. A., S. Dickinson, M. J. McPhaden, and G. C. Johnson, 2001: Ocean currents evident in satellite wind data. *Geophys. Res. Lett.,* **28,** 2469–2472.

Kennan, S. C., and P. J. Flament, 2000: Observations of a tropical instability vortex. *J. Phys. Oceanogr.,* **30,** 2277–2301.

Kummerow, C., W. Barnes, T. Kozu, J. Shiue, and J. Simpson, 1998: The Tropical Rainfall Measuring Mission (TRMM) sensor package. *J. Atmos. Oceanic Technol.,* **15,** 808–816.

Lindzen, R. S., and S. Nigam, 1987: On the role of sea surface temperature gradients in forcing low-level winds and convergence in the tropics. *J. Atmos. Sci.,* **44,** 2418–2436.

Liu, W. T., 1988: Moisture and latent heat flux variabilities in the tropical Pacific derived from satellite data. *J. Geophys. Res.,* **93,** 6749–6760.

——, W. Tang, and P. P. Niiler, 1991: Humidity profiles over the ocean. *J. Climate,* **4,** 1023–1034.

——, X. Xie, P. S. Polito, S.-P. Xie, and H. Hashizume, 2000: Atmospheric manifestation of tropical instability wave observed by QuikSCAT and Tropical Rain Measuring Mission. *Geophys. Res. Lett.,* **27,** 2545–2548.

McPhaden, M. J., and Coauthors, 1998: The tropical ocean–global atmosphere (TOGA) observing system: A decade of progress. *J. Geophys. Res.,* **103,** 14 169–14 240.

Mitchell, T. P., and J. M. Wallace, 1992: The annual cycle in equatorial convection and sea surface temperature. *J. Climate,* **5,** 1140–1156.

Oppenheimer, A. V., and R. A. Schafer, 1975: *Digital Signal Processing.* Prentice Hall, 360 pp.

Philander, S. G. H., D. Gu, D. Halpern, G. Lambert, N.-C. Lau, T. Li, and R. C. Pacanowski, 1996: Why the ITCZ is mostly north of the equator. *J. Climate,* **9,** 2958–2972.

Polito, P. S., J. P. Ryan, W. T. Liu, and F. P. Chavez, 2001: Ocean and atmospheric anomalies of tropical instability waves. *Geophys. Res. Lett.,* **28,** 2233–2236.

Qiao, L., and R. H. Weisberg, 1995: Tropical instability wave kinematics: Observations from the Tropical Instability Wave Experiment. *J. Geophys. Res.,* **100,** 8677–8693.

Spencer, M. W., C. Wu, and D. G. Long, 1997: Tradeoffs in the design of a spaceborne scanning pencil beam scatterometer: Application to SeaWinds. *IEEE Trans. Geosci. Remote Sens.,* **35,** 115–126.

Sweet, W., R. Fett, J. Kerling, and P. LaViolette, 1981: Air–sea interaction effects in the lower troposphere across the north wall of the Gulf Stream. *Mon. Wea. Rev.,* **109,** 1042–1052.

Tomas, R. A., J. R. Holton, and P. J. Webster, 1999: The influence of cross-equatorial pressure gradients on the location of near-equatorial convection. *Quart. J. Roy. Meteor. Soc.,* **125,** 1107–1127.

Wai, M. M.-K., and S. A. Stage, 1989: Dynamical analysis of marine atmospheric boundary layer structure near the Gulf Stream oceanic front. *Quart. J. Roy. Meteor. Soc.,* **115,** 29–44.

Wallace, J. M., T. P. Mitchell, and C. Deser, 1989: The influence of sea-surface temperature on surface wind in the eastern equatorial Pacific: Seasonal and interannual variability. *J. Climate,* **2,** 1492–1499.

Xie, S.-P., and S. G. H. Philander, 1994: A coupled ocean–atmosphere model of relevance to the ITCZ in the eastern Pacific. *Tellus,* **46A,** 340–350.

——, M. Ishiwatari, H. Hashizume, and K. Takeuchi, 1998: Coupled ocean–atmospheric waves in the equatorial front. *Geophys. Res. Lett.,* **25,** 3863–3866.

Zhang, G. J., and M. J. McPhaden, 1995: The relationship between sea surface temperature and latent heat flux in the equatorial Pacific. *J. Climate,* **8,** 589–605.